RSC Advances

PAPER

View Article Online
View Journal | View Issue

Cite this: *RSC Adv.*, 2023, **13**, 10681

Facile synthesis approach of bifunctional Co–Ni–Fe oxyhydroxide and spinel oxide composite electrocatalysts from hydroxide and layered double hydroxide composite precursors†

Sho Kitano, *[a] Yuki Sato, [b] Reiko Tagusari,[b] Ruijie Zhu,[b] Damian Kowalski,[c] Yoshitaka Aoki [a] and Hiroki Habazaki *[a]

Zinc–air batteries (ZABs) are promising candidates for the next-generation energy storage systems, however, their further development is severely hindered by kinetically sluggish oxygen evolution reaction (OER) and oxygen reduction reaction (ORR). Facile synthesis approaches of highly active bifunctional electrocatalysts for OER and ORR are required for their practical applications. Herein, we develop a facile synthesis procedure for composite electrocatalysts composed of OER-active metal oxyhydroxide and ORR-active spinel oxide containing Co, Ni and Fe from composite precursors consisting of metal hydroxide and layered double hydroxide (LDH). Both hydroxide and LDH are simultaneously produced by a precipitation method with a controlled molar ratio of Co^{2+}, Ni^{2+} and Fe^{3+} in the reaction solution, and calcination of the precursor at a moderate temperature provides composite catalysts of metal oxyhydroxides and spinel oxides. The composite catalyst shows superb bifunctional performances with a small potential difference of 0.64 V between a potential of 1.51 V *vs.* RHE at 10 mA cm^{-2} for OER and a half-wave potential of 0.87 V *vs.* RHE for ORR. The rechargeable ZAB assembled with the composite catalyst as an air-electrode exhibits a power density of 195 mA cm^{-2} and excellent durability of 430 hours (1270 cycles) of a charge–discharge cycle test.

Received 19th December 2022
Accepted 13th March 2023

DOI: 10.1039/d2ra08096f

rsc.li/rsc-advances

Introduction

With the rapidly growing demands for renewable energy, rechargeable zinc–air batteries (ZABs) have caught great attention due to their considerable energy density, low cost, safety, and high theoretical energy storage capacity (1218 W h kg^{-1}).[1,2] However, the greatest challenges for ZABs are poor cycle life and high overpotentials due to the kinetically sluggish oxygen evolution reaction (OER) and the oxygen reduction reaction (ORR) at the cathode in alkaline media. The performances of current ZABs hardly satisfy the requirements of practical applications.[3–5] Thus, tremendous efforts have been devoted to developing highly active bifunctional OER and ORR electrocatalysts.[6–10] Currently, Ru and Pt-based precious metal electrocatalysts have been reported as the best OER and ORR catalysts.[11,12] Although Pt-based catalysts are the best ORR catalysts, they are ineffective for OER. Likewise, the most active catalysts for the OER do not offer the best ORR catalysis performance. Calculation studies reported that the intrinsic activities for OER and ORR depend on the adsorption energy of intermediates on active sites, and the scaling relationship between the adsorption energy of intermediates prevents any compound with a single site from being both ORR and OER active.[13,14] Thus, combining an ORR active catalyst with an OER active catalysts have been examined to obtain bifunctional composite catalysts as another approach.[15] Because scarcity and high cost are hindered commercial applications of the noble metal compounds, there has been a great deal of research effort to develop inexpensive, robust, and efficient bifunctional electrocatalysts for rechargeable ZABs. Abundant Co-based multi transition metal compounds, including metal oxyhydroxides and spinel oxides, are expected as candidates of OER and ORR electrocatalysts[16] which have shown higher performances than those of monometallic ones.[17]

Metal oxyhydroxides have attracted much attention as an electrocatalyst for OER. While the OER activities of monometallic CoOOH are very low, including other transition metals

[a]*Division of Applied Chemistry, Faculty of Engineering, Hokkaido University, Sapporo, Hokkaido 060-8628, Japan. E-mail: skitano@eng.hokudai.ac.jp; habazaki@eng.hokudai.ac.jp; Tel: +81-92-802-6735; +81-92-802-6874*

[b]*Graduate School of Chemical Sciences and Engineering, Hokkaido University, Sapporo, Hokkaido 060-8628, Japan*

[c]*Biological and Chemical Research Centre (CNBCh), Faculty of Chemistry, University of Warsaw, ul. Żwirki i Wigury 101, 02-089, Warsaw, Poland*

† Electronic supplementary information (ESI) available. See DOI: https://doi.org/10.1039/d2ra08096f

such as Fe and Ni has drastically enhanced the performances.[18–20] Since the performances of multi-metal oxyhydroxide deeply depends on the kinds and compositions of metals, precise control of metal composition results in outstanding catalytic activities. A metal oxyhydroxide composed of Co, Ni, and Fe has exhibited higher OER activates than RuO_2 electrocatalyst;[18,20,21] trimetallic oxyhydroxides are promising materials for OER due to their composition versatility. Spinel oxides are one of the most extensively studied electrocatalysts for ORR.[22] Many researchers reported that Co_3O_4 nanoparticles loaded on carbon materials such as nitrogen-doped reduced graphene oxide[23,24] and carbon nanotube[25,26] showed superb ORR activities. Furthermore, Co-based spinel oxides with partial substitution of Ni and Fe have exhibited great potential in enhancing ORR activities,[27–29] indicating advantages of multi metallic composition to improve activities for spinel oxide electrocatalysts as well.

The composites of metal oxyhydroxide and spinel oxide composed of Co, Ni and Fe are expected to be highly active bifunctional electrocatalysts for ZABs, however, very few studies have been reported for OER and ORR.[30] In addition, the synthesis procedures should be as simple as possible without complicated operations from the viewpoint of practical applications. It is known that hydroxides can be converted to oxyhydroxides and layered double hydroxides (LDHs) to spinel oxides by calcination at moderate temperatures.[31–34] On the other hand, some studies have reported the formation of metal hydroxides as a byproduct in the synthesis of LDH.[35,36] Therefore, we expect that composite precursors of multi-metal hydroxides and LDHs are synthesized by the precipitation method and that calcination of the precursors at an appropriate temperature yields the composite of metal oxyhydroxide and spinel oxide, providing highly active bifunctional electrocatalysts (Scheme 1).

In this study, composite precursors of multi-metal hydroxides and LDHs containing Co, Fe and Ni are synthesized by a simple precipitation method and then calcined to synthesize oxyhydroxide and spinel oxide composite catalysts. The crystal structures of the precursors and catalysts are controlled by examining the metal composition and calcination temperature, and the synthesized catalysts are applied to OER and ORR in highly concentrated alkaline solutions. The catalysts are also applied as gas diffusion electrodes in half-cell and ZAB, and their activity and durability are investigated.

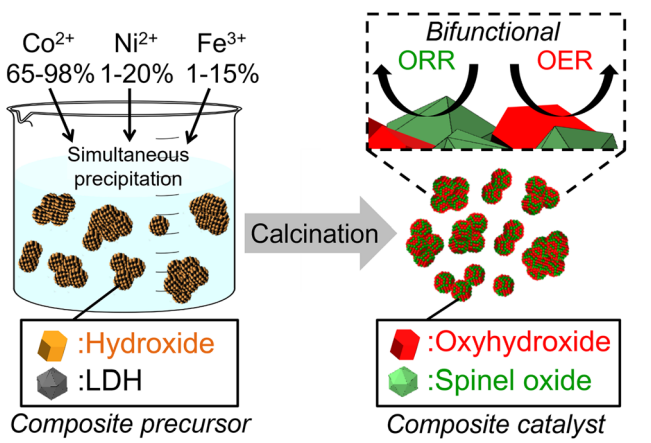

Scheme 1 Illustration of synthesis of bifunctional composite electrocatalyst of metal oxyhydroxide and spinel oxide from composite precursors of hydroxide and LDH.

Experimental

Catalyst preparation

All of the chemicals were used as received without further purification. All precursors were prepared by a precipitation method. The desired amounts of $Co(NO_3)_2 \cdot 6H_2O$, $Ni(NO_3)_2 \cdot 6H_2O$ and $Fe(NO_3)_3 \cdot 9H_2O$ (Kanto Chemical Co., Inc.), of which the total metal concentration corresponding to 0.1 mol dm^{-3} aqueous solution, were dissolved in 150 cm^3 pure water to obtain a transparent homogeneous solution. A 1.0 mol dm^{-3} KOH solution was quickly added in the above solution with vigorous stirring and then precipitation formed. The suspension was kept stirring for 1 h under the atmosphere, followed by filtration and washing with pure water and ethanol. The precipitation was dried *in vacuo* at room temperature for several hours, and then the precursors were obtained. The precursors were calcined at 100, 150 and 200 °C for 12 h under O_2 gas, and then the catalysts were obtained. Hereafter, the precursors and catalysts are designated $Co_XNi_YFe_Z$ and $Co_XNi_YFe_Z$ (T), respectively, where X, Y and Z means metal ratio in the samples determined by energy-dispersive X-ray spectroscopy (EDS) measurement ($X + Y + Z = 100$) and T means calcination temperature in degrees Celsius.

Characterization

The phase of samples was examined by X-ray powder diffraction (XRD, Rigaku, Ultima IV) using Cu Kα radiation (λ = 0.15418 nm, $U = 40$ kV, $I = 20$ mA). Morphology of the prepared samples was observed using a low-voltage scanning electron microscope (SEM, Zeiss, Sigma-500) operated at 1.5 kV. The morphology and composition of the samples were also analyzed using a scanning transmission electron microscope (STEM, JEOL, JEM-ARM200F) with EDS facilities. The metal composition of catalysts was also determined by analyzing solution of the samples dissolved in acid using the inductively coupled plasma atomic emission spectroscopy (ICP-AES) (Shimadzu, ICPE-9000). The specimens of electrodes for cross-section observation were prepared using a cross-section polisher (JEOL, IB-19530CP).

Electrochemical measurement

The electrocatalytic activity was evaluated by the rotating disk electrode (RDE; Pine Instrument Co. Ltd.) system using the catalyst-loaded glassy carbon disk electrode. For the preparation of catalyst inks, 50 mg of the prepared catalysts and carbon conductive additive (Acetylene black) with a 5 : 1 mass ratio were dispersed ultrasonically in a mixture of 0.2 mL of 5 wt% Na^+-exchanged Nafion solution and 4.8 mL of iso-propanol. Nafion was added as a binder and neutralized before dispersion to prevent the catalysts from undergoing acidic dissolution due to

the lower pH of the Nafion binder.[21] The ink (5 μL) was coated on the glassy carbon disk electrode. The electrochemical measurements were carried out using a three-electrode system connected with VersaSTAT 4 potentiostat/galvanostat (Princeton Applied Research). A platinum coil and Hg/HgO/4 mol dm^{-3} KOH were used as counter and reference electrodes, respectively. All measurements were carried out at room temperature in a 4 mol dm^{-3} KOH aqueous solution (pH = 14). The electrocatalytic activity was evaluated using linear sweep voltammetry (LSV) with a potential sweep rate of 1 mV s^{-1}. The electron transfer number during ORR was evaluated by the RRDE method under the ring electrode potential of 1.4 V *vs.* RHE.[37,38] The potential was converted from the Hg/HgO/4 mol dm^{-3} KOH reference scale to the RHE using the following equation:

$$E \text{ vs. RHE} = E \text{ vs. Hg/HgO/4 mol dm}^{-3} \text{ KOH} + 0.926 \quad (1)$$

Evaluation of air electrode performances

The long-term durability of the prepared catalyst was evaluated using the gas-diffusion electrode (GDE), which consisted of the hydrophobic gas-diffusion layer (GDL), catalyst layer (CL), and Ni mesh current collector (Niraco). The GDE experiments were conducted based on the previous reports.[39,40] The hydrophobic gas-diffusion layer (GDL) was prepared from a mixture of 70 wt% carbon black (TOKAI CARBON, #3800) and 30 wt% polytetrafluoroethylene (PTFE). The resultant carbon/PTFE mixture was rolled in several steps to obtain 0.3 mm-thin sheets. After drying the prepared sheet at 60 °C, the GDL was cut out from the sheet into a 12 mm diameter circle, followed by heating at 334 °C for 1 h under N_2 flow. Catalyst layers on the GDL were prepared by spraying the catalyst ink in circle with 8 mm diameter, which was a mixture of the prepared catalyst, carbon additive, 5 wt% Na^+-exchanged Nafion solution, water and iso-propanol. The ratio of catalyst, carbon and Nafion was controlled to be 45 : 45 : 10 in wt% in the resultant catalyst layer. The catalyst was assembled with the GDL with the loading amount of 7 mg cm^{-2}, followed by pressing onto the Ni mesh current collector. The prepared GDE and PTFE gasket O-ring were held in a Swagelok union (PFA-820-6) connected with stainless and perfluoroalkoxy alkane (PFA) pipes. The electrochemical cell for the GDE test consisted of a Pt wire, a Hg/HgO electrode, and a 4 mol dm^{-3} KOH aqueous solution as a counter electrode, a reference electrode, and an electrolyte solution, respectively. The charge–discharge tests were conducted at 40 °C in the incubator. The air electrode was exposed to ambient air without forced flow. Charge and discharge curves were obtained by monitoring the potential of the air electrode using a galvanostat (Biologic, VSP). The charge–discharge cycle test was conducted by applying 20 mA cm^{-2} for 1 h with an open circuit potential of 3 min interval for each cycle. The aqueous ZABs were constructed by employing a 500 μm thick zinc foil as the anode, the prepared GDE as the air cathode and 6 mol dm^{-3} KOH-based electrolyte containing 0.2 mol dm^{-3} zinc acetate. The ZAB experiments were conducted in an atmospheric environment at room temperature.

Results and discussion

Preparation of precursors

Initially, we examined to prepare composite precursors of multimetal hydroxide and LDH from aqueous solutions containing more than two kinds of metal ions by the precipitation method and investigated the effect of the molar ratio of metal ions in the solution on the obtained precursors. Fig. 1 shows the XRD patterns of unary, binary and ternary metal precursors prepared by the precipitation method and CoNi-LDH as a reference sample synthesized by a topochemical oxidation method.[41] The unary Co_{100} showed the pattern assignable to β-$Co(OH)_2$, indicating that the precipitation method in the solution containing only Co ion yielded the Co hydroxide with no other products. The binary $Co_{80}Ni_{20}$ and $Co_{94}Fe_6$ precursors showed patterns assignable to LDH in addition to β-$Co(OH)_2$. Previous studies have reported that LDH samples are synthesized by the precipitation method,[33,42] in which alkaline reagents are added to aqueous solutions containing divalent and trivalent metal ions. The LDH can be obtained only when the ratio of trivalent metal ions is 20–33% of total metal ions,[34] otherwise metal hydroxides are simultaneously formed as by-products. Thus, precursors in which hydroxide and LDH coexisted could be prepared by controlling the ratio of trivalent metal ions in the reaction solution to less than 20%. In the $Co_{80}Ni_{20}$ precursor,

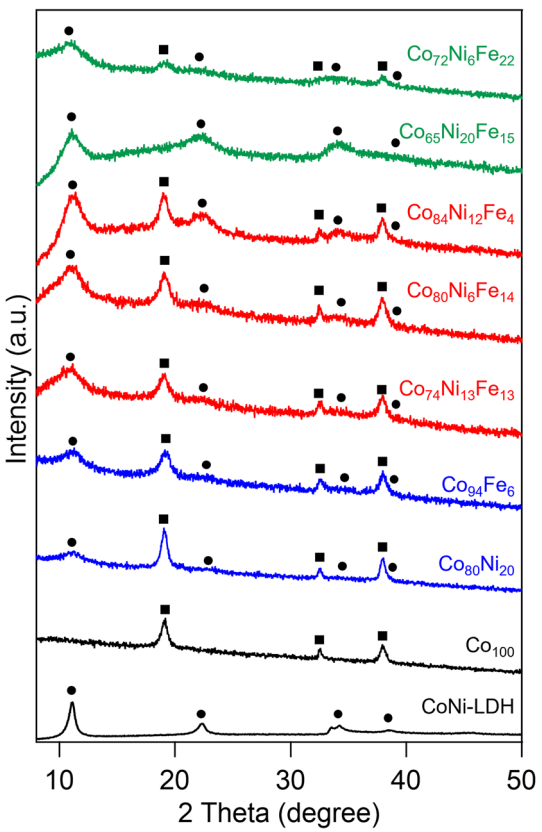

Fig. 1 XRD patterns of the precursors with different metal composition ratio, Co_{100} and CoNi-LDH reference (circle: LDH, square: hydroxide).

LDH was also formed in addition to hydroxide even though both ions are divalent. The result was probably due to partially oxidation of the divalent metal ions by dissolved oxygen in the solution,[43] resulting in the formation of the LDH. The ternary precursors showed different XRD patterns depending on the metal ion ratio. Both the hydroxide and LDH formed in the $Co_{74}Ni_{13}Fe_{13}$, $Co_{80}Ni_6Fe_{14}$ and $Co_{84}Ni_{12}Fe_4$ precursors. The precursors with Ni ratios of 20% or higher ($Co_{65}Ni_{20}Fe_{15}$) did not show the pattern assignable to hydroxide, but only that to LDH. Patterns assignable to hydroxide and LDH were also observed for the $Co_{72}Ni_6Fe_{22}$ precursor. However, the catalyst obtained by calcination of the $Co_{72}Ni_6Fe_{22}$ precursor showed only the pattern assignable to the spinel oxide (Fig. S1†), indicating that the $Co_{72}Ni_6Fe_{22}$ was not appropriate as the precursor. Because the samples calcined at 150 °C for the $Co_{74}Ni_{13}Fe_{13}$, $Co_{80}Ni_6Fe_{14}$ and $Co_{84}Ni_{12}Fe_4$ showed the patterns assignable to oxyhydroxide and spinel oxide as discussed below, the hydroxide and LDH composite precursors can be obtained when the composition ratio of Ni and Fe is less than 15 at%. These results indicated that the precipitation method in the aqueous solution containing two or three metal ions with the appropriate molar ratio could yield precursors containing both hydroxide and LDH. From the SEM-EDX measurements, the composition metal ratio of the precursors showed a larger ratio of Fe to that in the reaction solution (Table S1†). This was probably due to the solubility of the metal ions, *i.e.*, Fe^{3+} has a much lower solubility than that of Ni^{2+} and Co^{2+}. The metal composition was also measured by analyzing solution of the samples dissolved using ICP-AES and similar results to those from SEM-EDX measurement were observed (Table S2†).

Effects of calcination temperature

It is known that metal hydroxides and LDHs change to metal oxyhydroxides and spinel oxides by calcination at low temperature,[18,32,33] respectively, and oxyhydroxides convert to spinel oxides at high temperature.[31] In this study, since the oxyhydroxide and spinel oxide must coexist after calcination, we investigated the effect of calcination on the precursors to synthesize the metal oxyhydroxide and spinel oxide composite catalysts. Fig. 2 shows the XRD patterns of the $Co_{74}Ni_{13}Fe_{13}$, Co_{100} and samples obtained by calcining them at 100, 150 and 200 °C. The Co_{100} samples calcined at 100 and 200 °C showed the patterns assignable to β-CoOOH and Co_3O_4, respectively. The results indicated that the crystal structure of $Co(OH)_2$ changed depending on the calcination temperature, which were consistent with the previous studies.[31] The pattern of the $Co_{74}Ni_{13}Fe_{13}$ (100) showed peaks assignable to oxyhydroxide, indicating that metal hydroxide of precursor changed to oxyhydroxide. Moreover, the peak around 11° disappeared and no peaks assignable to spinel oxide were observed for the $Co_{74}Ni_{13}Fe_{13}$ (100), suggesting the collapse of the structure of LDH and formation of amorphous oxide at 100 °C. The $Co_{74}Ni_{13}Fe_{13}$ (150) showed both patterns assignable to oxyhydroxide and spinel oxide. The results indicated that the crystalline structure of oxyhydroxide was maintained and spinel oxide formed from amorphous oxide at 150 °C. Previous studies have reported that

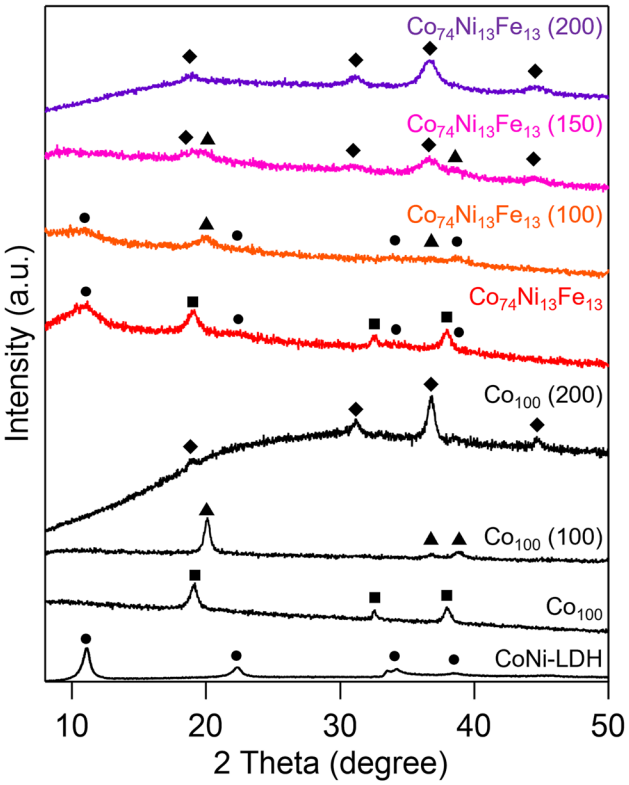

Fig. 2 XRD patterns of the $Co_{74}Ni_{13}Fe_{13}$ precursor, Co_{100}, corresponding calcined samples and CoNi-LDH reference (circle: LDH, square: hydroxide, triangle: oxyhydroxide, diamond: spinel oxide).

calcination changes LDHs to spinel oxides *via* amorphous oxides,[33] which corresponded to the results in this study. In the $Co_{74}Ni_{13}Fe_{13}$ (200), the peaks assignable to oxyhydroxide disappeared and the pattern of spinel oxide was only observed, suggesting that the oxyhydroxide converted and the whole sample changed to spinel oxide at 200 °C. Therefore, calcination at 150 °C is the best condition for the synthesis of oxyhydroxide and spinel oxide composite catalysts. Because the $Co_{80}Ni_6Fe_{14}$ (150) and $Co_{84}Ni_{12}Fe_4$ (150) also showed the patterns assignable to both oxyhydroxide and spinel oxide (Fig. S2†), we concluded that the composite catalysts of oxyhydroxide and spinel oxide were successfully synthesized by calcination of the composite precursor of hydroxide and LDH at the adequate temperature.

Characterization of oxyhydroxide and spinel oxide composite catalyst

We investigated the morphology and composition of the composite catalyst. Fig. 3(a)–(c) shows SEM and TEM images of $Co_{74}Ni_{13}Fe_{13}$ (150). TEM and SEM observations revealed that the $Co_{74}Ni_{13}Fe_{13}$ (150) catalyst showed an aggregated morphology consisting of oxyhydroxide and spinel oxide primary nanoparticles with diameters of several nanometers. From the high-resolution TEM observation, lattice fringes of primary nanoparticles coincided with the (003) plane of the oxyhydroxide and the (311) plane of the spinel oxide (Fig. 3(c)).

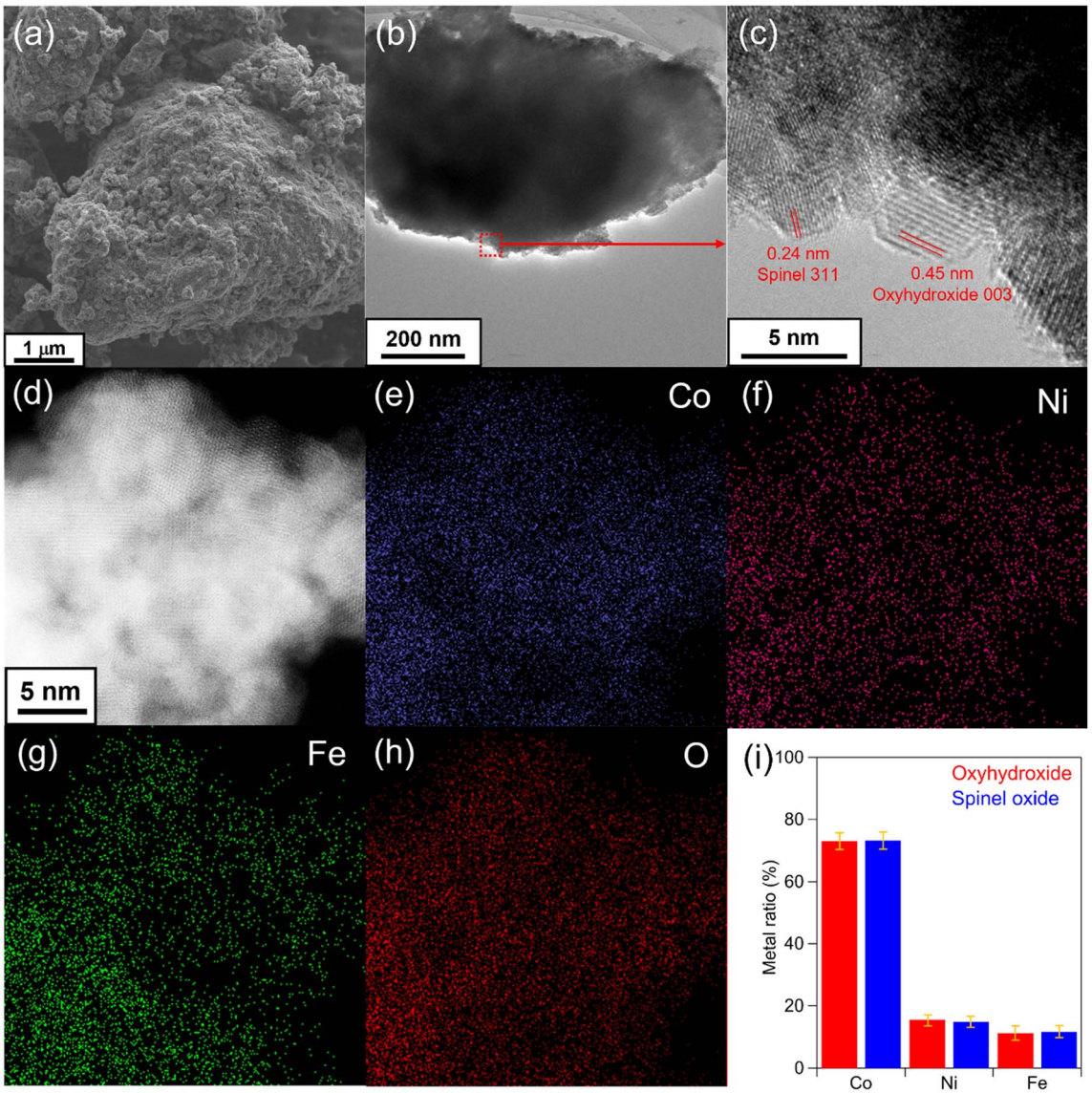

Fig. 3 (a) SEM and (b), (c)TEM images of the $Co_{74}Ni_{13}Fe_{13}$ (150) catalyst. (d) HAADF-STEM image and STEM-EDX maps for (e) Co–K, (f) Ni–K, (g) Fe–K, (h) O–K. (i) Metal composition ratio of oxyhydroxide and spinel oxide constituting the $Co_{74}Ni_{13}Fe_{13}$ (150) catalyst.

These results indicated that $Co_{74}Ni_{13}Fe_{13}$ (150) was the catalyst with the mixture of oxyhydroxide and spinel oxide. The STEM-EDX mapping exhibited a uniform distribution of Co, Ni, Fe and O in the catalyst, indicating that metal elements homogeneously existed in the nanoparticles (Fig. 3(d)–(h)). Fig. 3(i) shows metal ratios of the oxyhydroxide and spinel oxide determined by STEM-EDX measurements from each primary particle identified by the lattice fringes. The oxyhydroxide and spinel oxide had almost identical average metal ratio; Co:75%, Ni: 14%, Fe: 11%, with small ranges of about ±4%, which were almost the same as the overall metal ratio obtained by SEM-EDX. The results indicated that the catalyst had uniform distribution of metals in both oxyhydroxide and spinel oxide nanoparticles with similar compositions. We also confirmed that metal ratio of catalysts coincided with that of the corresponding precursors.

Effects of crystalline structure on OER and ORR performances

We applied the $Co_{74}Ni_{13}Fe_{13}$ (T) catalysts to ORR and OER to investigate the effects of crystal structure on catalytic performances. Fig. 4(a) shows polarization curves of the $Co_{74}Ni_{13}Fe_{13}$ (T) catalysts and a commercial Pt/C, which is the representative ORR catalyst, for ORR in an O_2-saturated 4 mol dm^{-3} KOH solution. The $Co_{74}Ni_{13}Fe_{13}$ (200) showed superior electrocatalytic activities toward ORR with an onset potential of 0.93 V *vs.* RHE and a half-wave potential ($E_{1/2}$) of 0.89 V *vs.* RHE, much more positive than those of $Co_{74}Ni_{13}Fe_{13}$ (150) (onset potential, 0.92 V *vs.* RHE; $E_{1/2}$, 0.87 V *vs.* RHE) and $Co_{74}Ni_{13}Fe_{13}$ (100) (onset potential, 0.87 V *vs.* RHE; $E_{1/2}$, 0.81 V *vs.* RHE). The difference in half-wave potential between the $Co_{74}Ni_{13}Fe_{13}$ (200) and the commercial Pt/C (onset potential, 1.02 V *vs.* RHE; $E_{1/2}$, 0.94 V *vs.* RHE) was only about 0.05 V. The $Co_{74}Ni_{13}Fe_{13}$ (200) exhibited smaller Tafel slope (33 mV dec^{-1}) than those of

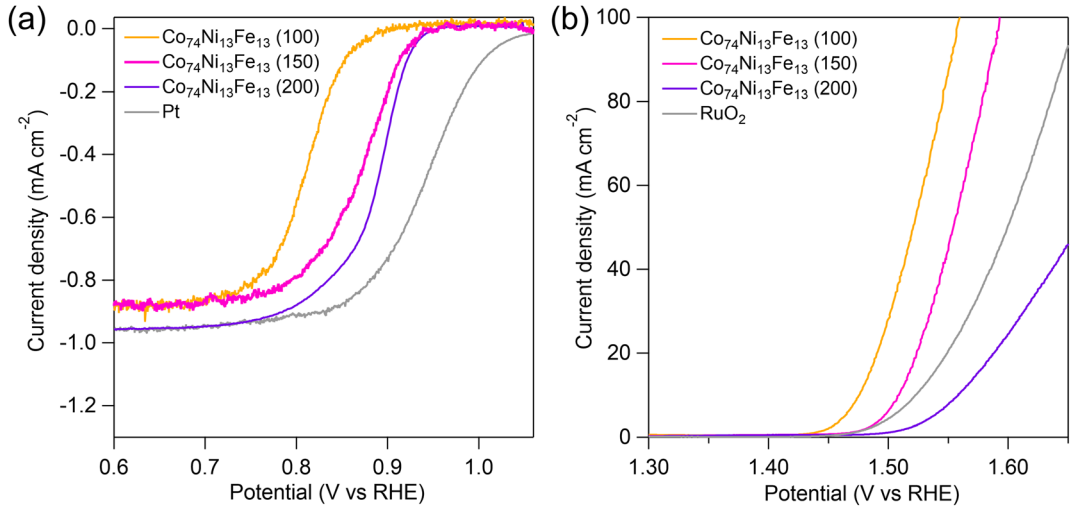

Fig. 4 Polarization curves of the calcined $Co_{74}Ni_{13}Fe_{13}$ catalysts, Pt/C and RuO_2 for (a) ORR and (b) OER in an O_2-saturated 4 mol dm^{-3} KOH solution.

$Co_{74}Ni_{13}Fe_{13}$ (150) (44 mV dec^{-1}) and $Co_{74}Ni_{13}Fe_{13}$ (100) (56 mV dec^{-1}) (Fig. S3†). All $Co_{74}Ni_{13}Fe_{13}$ (T) catalysts showed high electron transfer numbers ($n > 3.5$) (Fig. S4†). For ORR activity, the order of activity was $Co_{74}Ni_{13}Fe_{13}$ (200) > $Co_{74}Ni_{13}Fe_{13}$ (150) > $Co_{74}Ni_{13}Fe_{13}$ (100). Fig. 4(b) shows polarization curves of the catalysts and a commercial RuO_2 for OER in a 4 mol dm^{-3} KOH solution. The $Co_{74}Ni_{13}Fe_{13}$ (100) exhibited the lowest overpotential (0.25 V) at 10 mA cm^{-2} among the catalysts, followed by $Co_{74}Ni_{13}Fe_{13}$ (150) (0.28 V) and $Co_{74}Ni_{13}Fe_{13}$ (200) (0.33 V). The $Co_{74}Ni_{13}Fe_{13}$ (100) and $Co_{74}Ni_{13}Fe_{13}$ (150) showed higher activity than that of even RuO_2. Moreover, the Tafel slope of $Co_{74}Ni_{13}Fe_{13}$ (100) (38 mV dec^{-1}) and $Co_{74}Ni_{13}Fe_{13}$ (150) (41 mV dec^{-1}) were smaller than those of the $Co_{74}Ni_{13}Fe_{13}$ (200) (62 mV dec^{-1}) and RuO_2 (61 mV dec^{-1}) (Fig. S5†), also indicating higher activities of the $Co_{74}Ni_{13}Fe_{13}$ (100) and $Co_{74}Ni_{13}Fe_{13}$ (150). For OER activity, the order of activity was $Co_{74}Ni_{13}Fe_{13}$ (100) > $Co_{74}Ni_{13}Fe_{13}$ (150) > $Co_{74}Ni_{13}Fe_{13}$ (200). Therefore, the higher the calcination temperature, the higher the activity for ORR, and the lower the activity for OER.

It has been reported that multi-metal oxyhydroxides containing Co and Fe or Ni and Fe show high OER activities, but low ORR activities,[44] while spinel oxides show high ORR activities.[45] Some spinel oxides have exhibited high OER activity; however, multi-metal oxyhydroxides have exhibited higher OER activities than spinel oxides in many reports.[46,47] Since the $Co_{74}Ni_{13}Fe_{13}$ (100) and (150) containing the oxyhydroxide showed lower overpotential and Tafel slopes than the $Co_{74}Ni_{13}Fe_{13}$ (200) composed only of spinel oxide, OER activities of the oxyhydroxides were higher than those of spinel oxides in this catalyst system. The unary Co oxyhydroxide, Co_{100} (100), showed higher OER and lower ORR activity than the unary Co spinel oxide, Co_{100} (200) (Fig. S6†). Therefore, the results indicated that the composite catalysts calcined at lower temperature with larger part of oxyhydroxide showed higher OER and lower ORR activity, and the catalysts calcined at higher temperature with larger part of spinel oxide showed higher ORR and relatively lower OER activity. The catalytic performances of a physically mixed sample of spinel oxide and oxyhydroxide was evaluated to compare with the activities of composite catalyst (Fig. S7†). The $Co_{74}Ni_{13}Fe_{13}$ (150) showed higher ORR and OER activities than those of the physically mixed sample. The results were probably attributed to the difference in dispersion of spinel oxide and oxyhydroxide in the catalysts. The $Co_{74}Ni_{13}Fe_{13}$ (150) was the composite of well-dispersed primary nanoparticles of spinel oxide and oxyhydroxide (Fig. 3), while the simply mixed sample would be composed of their secondary particles. Therefore, the spinel oxide and oxyhydroxide composite catalysts formed from the composite precursors provided superior bifunctional ORR and OER performances.

The overall oxygen electrode activities are often evaluated by the value of ΔE, which is defined as a potential difference between an OER potential at 10 mA cm^{-2} ($E_{j=10}$) and $E_{1/2}$ for ORR. A lower ΔE value indicates better bifunctional catalytic performances. The $Co_{74}Ni_{13}Fe_{13}$ (150) showed the smaller ΔE of 0.64 V than those of the $Co_{74}Ni_{13}Fe_{13}$ (100) (ΔE = 0.67 V) and $Co_{74}Ni_{13}Fe_{13}$ (200) (ΔE = 0.67 V). Therefore, the $Co_{74}Ni_{13}Fe_{13}$ (150) showed both high ORR and OER activities due to coexisting of the oxyhydroxide and spinel oxide.

Effects of metal composition on OER and ORR activities

Because the composite catalysts with oxyhydroxide and spinel oxide showed high bifunctional activities for OER and ORR, we investigated the influences of metal composition on catalytic activities. Fig. 5 shows polarization curves of the composite catalysts with different metal compositions for ORR and OER in a 4 mol dm^{-3} KOH aqueous solution. The composite catalysts showed different ORR and OER activities depending on the metal composition. Comparing $Co_{74}Ni_{13}Fe_{13}$ (150) and $Co_{80}Ni_6Fe_{14}$ (150), of which the Fe content was almost the same and the Ni content was different, the $Co_{74}Ni_{13}Fe_{13}$ (150) showed higher ORR and OER activities ($E_{1/2}$ = 0.87 V, $E_{j=10}$ = 1.51 V *vs.* RHE) than those of $Co_{80}Ni_6Fe_{14}$ (150) ($E_{1/2}$ = 0.84 V, $E_{j=10}$ =

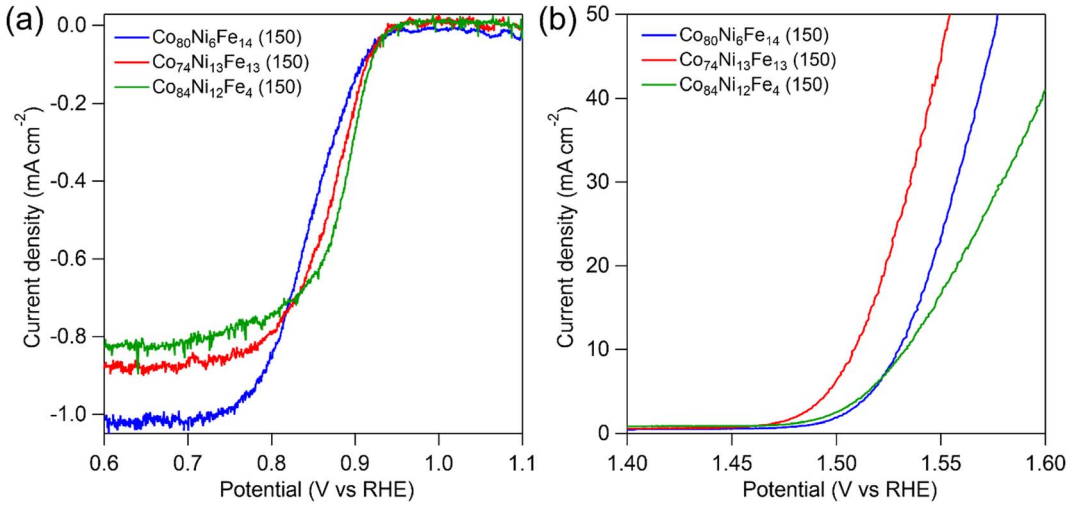

Fig. 5 Polarization curves of the composite catalysts with different composition ratio for (a) ORR and (b) OER in an O_2-saturated 4 mol dm^{-3} KOH solution.

1.53 V *vs.* RHE). The results suggested that inclusion of Ni enhanced activities for both ORR and OER. Comparing $Co_{74}Ni_{13}Fe_{13}$ (150) and $Co_{84}Ni_{12}Fe_4$ (150), of which the Ni content was almost the same and the Fe content was different, the $Co_{74}Ni_{13}Fe_{13}$ (150) catalysts showed lower ORR activities and higher OER activities than those of $Co_{80}Ni_6Fe_{14}$ (150) ($E_{1/2}$ = 0.89 V, $E_{j=10}$ = 1.54 V *vs.* RHE). The activity trends suggested that inclusion of Fe increased OER activities but decreased ORR activities. Comparing the bifunctional activities based on ΔE, the $Co_{74}Ni_{13}Fe_{13}$ (150) catalyst showed higher bifunctional performances (ΔE = 0.64 V) than those of $Co_{80}Ni_6Fe_{14}$ (150) (ΔE = 0.69 V) and $Co_{84}Ni_{12}Fe_4$ (150) (ΔE = 0.65 V). The $Co_{74}Ni_{13}Fe_{13}$ (150) catalyst showed the highest bifunctional performances among the catalysts in this study, which was even comparable to the state-of-the-art bifunctional catalysts (Table S3†). Therefore, control of metal composition achieved the excellent bifunctional OER and ORR performances of the oxyhydroxide and spinel oxide composite catalyst.

Air-electrode performances

For practical application of bifunctional OER and ORR catalysts to ZABs, gas diffusion air-electrodes were fabricated to achieve high reaction rates using O_2 in the atmosphere. We applied the $Co_{74}Ni_{13}Fe_{13}$ (150) catalyst to the air-electrode and examined the bifunctional performances and durability of the catalyst. Fig. 6(a) shows the charge–discharge cycle performance of $Co_{74}Ni_{13}Fe_{13}$ (150) in a 4 mol dm^{-3} KOH aqueous electrolyte at 40 °C. The durability of the $Co_{74}Ni_{13}Fe_{13}$ (150) catalyst was evaluated by chronopotentiometry approaches at the constant anodic and cathodic current density of 20 mA cm^{-2}. The fabricated air-electrode exhibited initial charge (OER) and discharge (ORR) potentials of 1.48 and 0.76 V *vs.* RHE, respectively, demonstrating a small total overpotential of 0.72 V. The total overpotential was maintained without any obvious deterioration even after more than 550 hours (260 cycles), showing excellent durability of the electrode for OER and ORR. Table S4† summarizes the comparison of the air-electrode performances with other recently reported results, indicating the superior activity and durability of the $Co_{74}Ni_{13}Fe_{13}$ (150) catalyst.

After 1000 hours, there was a performance deterioration, especially, the ORR performance significantly decreased (Fig. S8†). We conducted the XRD measurement and SEM observation for the electrode after the cycle test to clarify the cause of performance deterioration. The catalyst layer of air-electrode showed similar patterns assignable to the oxyhydroxide, spinel oxide and carbon conductive additive before and after the cycle test, indicating negligible change in crystalline structures of the catalyst (Fig. S9†). On the other hand, the intensity of the peak assignable to carbon at 26° was decreased. Fig. 6(b)–(g) shows surface and cross-section SEM images of the electrode before and after the cycle test. A large amount of carbon black disappeared, and more catalysts were exposed on the surface after the cycle test. The cross-section SEM observation after the cycle test revealed that more voids were formed in the catalyst layer of the electrode than before the test. Moreover, the morphology of carbon black in the gas diffusion layer was changed from a dense spherical to a hollow irregularly shape. The results clearly suggested that the carbon black was decomposed during the cycle test. Because carbon materials are thermodynamically decomposed under anodic conditions above 0.207 V *vs.* NHE,[48] the carbon black in the catalyst and gas diffusion layers corroded during the reaction. On the other hand, the change in the $Co_{74}Ni_{13}Fe_{13}$ (150) catalyst was negligible before and after the cycle test. The STEM observation clarified that oxyhydroxide and spinel oxide nanoparticles with corroded carbon conductive additives existed and no other compounds were observed after the cycle test (Fig. S10†). The ratio of metals in the oxyhydroxide and spinel oxide nanoparticles measured by STEM-EDX analysis was consistent with those before the reaction (Fig. S11†), and homogenous metal distribution in the nanoparticles was observed in the elemental mapping after the cycle test as well

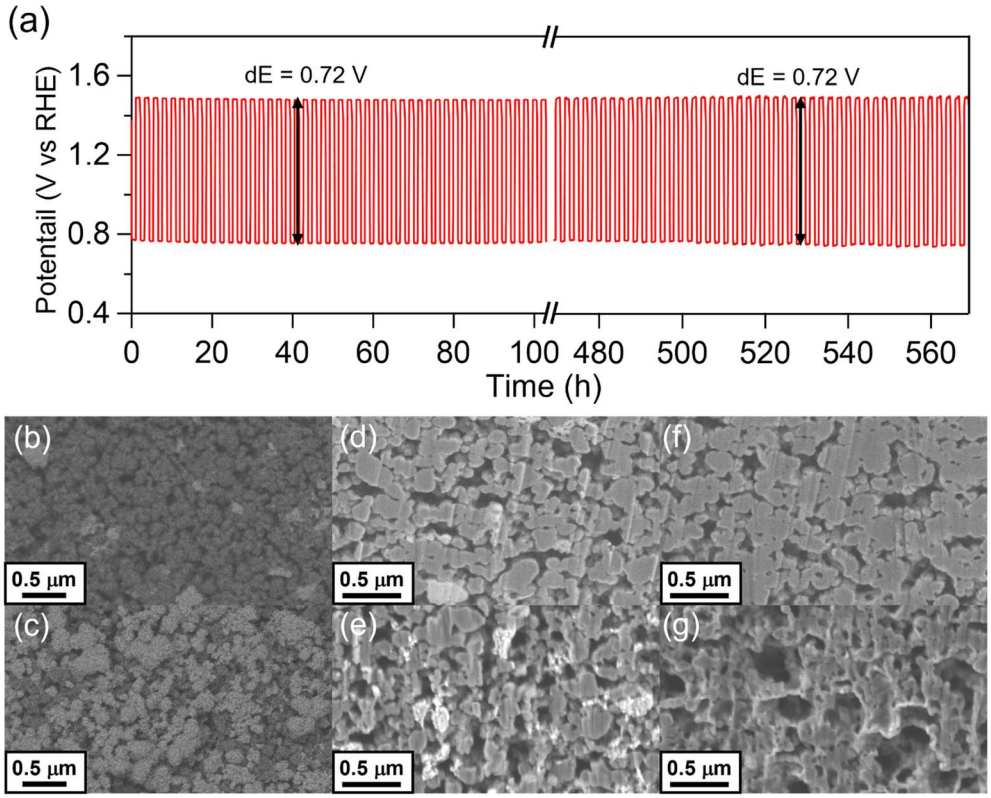

Fig. 6 (a) Charge–discharge cycle performance of the $Co_{74}Ni_{13}Fe_{13}$ (150) air-electrode at 20 mA cm^{-2} in 4 mol dm^{-3} KOH aqueous solution. Back scattering electron SEM images of the surface of the $Co_{74}Ni_{13}Fe_{13}$ (150) air-electrode (b) before and (c) after cycle test. Cross-section secondary electron SEM images of the catalyst layer (d) before and (e) after cycle test and gas-diffusion layer (f) before and (g) after cycle test.

(Fig. S12†). We analyzed residual metals in the electrolyte after durability test by ICP-AES and only a trace amount of dissolved metals, up to approximately 0.21% of the total catalyst, was detected even after long-term test of 1000 h (Table S5†). The results indicated that the effect of metal dissolution on the performance deterioration was negligible and the $Co_{74}Ni_{13}Fe_{13}$ (150) catalyst has high stability in the long-term test. Based on the results, the decrease in ORR performances was attributed to not the deterioration of the catalyst but corrosion of carbons in the catalyst and gas-diffusion layers. The corrosion of the carbon black in the catalyst and gas-diffusion layers caused the electrolyte solution to gradually penetrate through the air electrode to the gas phase during the cycle test, resulting in insufficient O_2 diffusion and a considerable decrease of ORR performances due to immersion of active sites at the three-phase boundary.[38] For OER process, OH^- is the substrate and the O_2 produced in the reaction was released not only to the gas side but also to the solution. Thus, the OER performances were not decreased as significantly as the ORR performances. The $Co_{74}Ni_{13}Fe_{13}$ (150) catalyst did not show significant change in the structure and composition after the cycle test, indicating excellent stability for OER and ORR. Therefore, the composite catalysts of oxyhydroxide and spinel oxide exhibited superb bifunctional activities and durability for OER and ORR, and fabrication with anti-corrosive conductive materials instead of carbons will achieve a longer lifetime for air-electrode performances.

Furthermore, we assembled an aqueous ZAB with Zn foil as the anode and $Co_{74}Ni_{13}Fe_{13}$ (150) as the air cathode in a solution containing 6 mol dm^{-3} KOH and 0.2 mol dm^{-3} zinc acetate. Fig. 7(a) shows the charge–discharge polarization curves of the $Co_{74}Ni_{13}Fe_{13}$ (150) and a physical mixture sample of Pt/C and RuO_2 (Pt–RuO_2). The ZAB with $Co_{74}Ni_{13}Fe_{13}$ (150) exhibited superior charge and discharge curves compared to those of the ZAB with Pt–RuO_2. The peak power density of $Co_{74}Ni_{13}Fe_{13}$ (150) and Pt–RuO_2 were 195 and 31.7 mW cm^{-2}, respectively, indicating that the $Co_{74}Ni_{13}Fe_{13}$ (150) electrode showed higher performances compared to the Pt–RuO_2 sample (Fig. 7(b)). The long-term durability of the rechargeable ZABs was evaluated through galvanostatic charge–discharge cycling (Fig. 7(c)). The total charge–discharge overpotential of $Co_{74}Ni_{13}Fe_{13}$ (150) upon cycling was only 0.65 V, which was much smaller than that of Pt–RuO_2 (0.89 V). The charge–discharge profile of $Co_{74}Ni_{13}Fe_{13}$ (150) was retained after 430 h (1270 cycles) while the performance of Pt–RuO_2 was rapidly deteriorated within 8 h. The performance of the ZAB with $Co_{74}Ni_{13}Fe_{13}$ (150) was comparable to that with state-of-the-art catalysts (Table S6†), demonstrating that the $Co_{74}Ni_{13}Fe_{13}$ (150) was highly suitable for rechargeable ZABs as a bifunctional electrocatalyst. The excellent bifunctional ORR and OER performances of the composite catalyst of oxyhydroxide and spinel oxide may be due to synergistic effects of the combination of materials. Elucidation of the synergistic effects would be a next challenge.

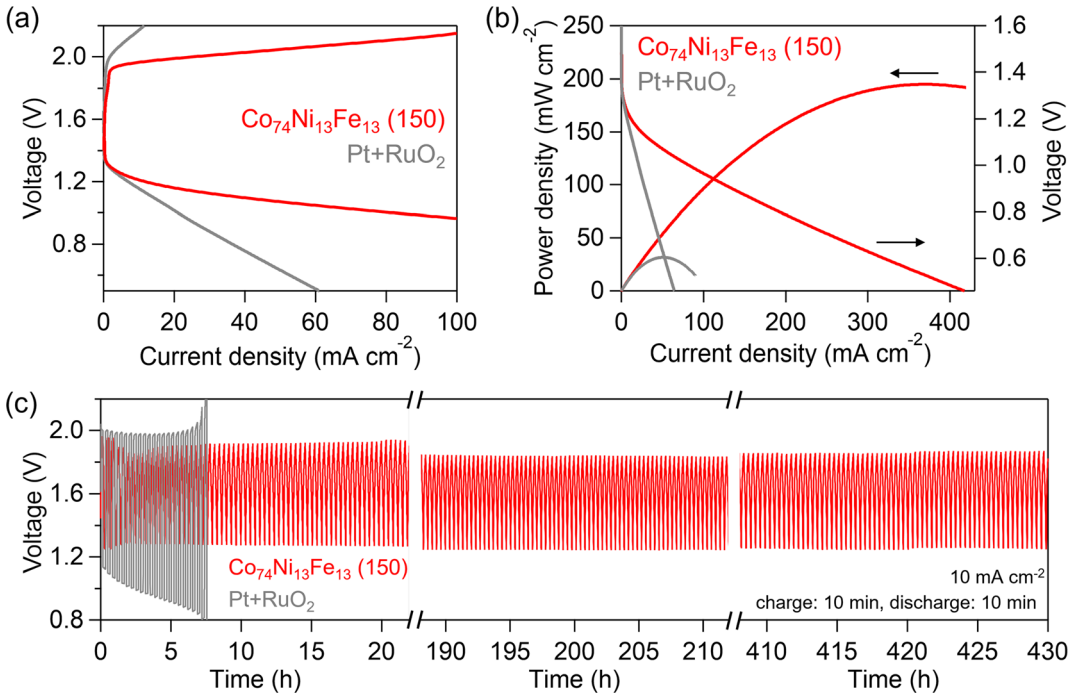

Fig. 7 (a) Charge and discharge polarization curves, (b) corresponding powder densities and (c) charge and discharge voltage profiles of ZABs with the $Co_{74}Ni_{13}Fe_{13}$ (150) (red) and Pt–RuO_2 (gray) air-electrodes.

Conclusion

In summary, we synthesized bifunctional OER and ORR composite electrocatalysts of metal oxyhydroxide and spinel oxide containing Co, Ni and Fe by calcination of hydroxide and LDH composite precursors prepared by a precipitation method. The composite precursors of metal hydroxide and LDH were prepared when both the Ni and Fe metal composition ratio was below 15 at%, and then calcination of the precursors at 150 °C yielded the composite catalysts of multi-metal oxyhydroxide and spinel oxide. The activities of composite catalysts depended on the metal composition; the inclusion of Ni enhanced activities for both ORR and OER and the inclusion of Fe increased OER activities but decreased ORR activities. The $Co_{74}Ni_{13}Fe_{13}$ (150) showed superb bifunctional performances with a small potential difference of 0.64 V due to high OER and ORR activities originating from the oxyhydroxide and spinel oxide, respectively. The $Co_{74}Ni_{13}Fe_{13}$ (150) also exhibited excellent durability of more than 550 h (260 cycles) for the air-electrode charge–discharge cycle evaluation with negligible change in crystalline structure and composition. The ZAB with $Co_{74}Ni_{13}Fe_{13}$ (150) demonstrated the power density of 195 mA cm^{-2} and excellent durability of 430 hours (1270 cycles) for the charge–discharge cycle test. The synthetic procedure of composite catalyst will contribute to opening up new opportunities for the development of air-electrodes for ZABs.

Author contributions

S. Kitano; conceptualization, supervision, visualization, resources, writing – review & editing, funding acquisition, methodology: Y. Sato; investigation, data curation, methodology: R. Tagusari; investigation: R. Zhu; investigation: D. Kowalski; investigation, methodology: Y. Aoki; investigation, methodology: H. Habazaki; conceptualization, supervision, visualization, resources, writing – review & editing, funding acquisition, methodology. All authors have given approval to the final version of the manuscript.

Conflicts of interest

The authors declare no competing financial interest.

Acknowledgements

Part of this study was conducted at the Multi-Quantum Beam High Voltage Electron Microscope Laboratory at Hokkaido University, supported by the Nanotechnology Platform Program of the Ministry of Education, Culture, Sports, Science and Technology (MEXT), Japan (A-19-HK-0003, A-20-HK-0002, A-21-HK-0035). We acknowledge funding by JSPS KAKENHI (22K05295) and the New Energy and Industrial Technology Development Organization (NEDO) grant number JPNP16001 (Research and Development Initiative for Scientific Innovation of New Generation Batteries (RISING2)), Japan. A part of this work was conducted at Laboratory of XPS analysis, Joint-use facilities, Hokkaido university.

References

1 J. Fu, Z. P. Cano, M. G. Park, A. Yu, M. Fowler and Z. Chen, Electrically Rechargeable Zinc-Air Batteries: Progress,

Challenges, and Perspectives, *Adv. Mater.*, 2017, **29**(7), 1604685, DOI: 10.1002/adma.201604685.

2 J. Fu, R. Liang, G. Liu, A. Yu, Z. Bai, L. Yang and Z. Chen, Recent Progress in Electrically Rechargeable Zinc-Air Batteries, *Adv. Mater.*, 2019, **31**(31), e1805230, DOI: 10.1002/adma.201805230.

3 S. Kitano, T. G. Noguchi, M. Nishihara, K. Kamitani, T. Sugiyama, S. Yoshioka, T. Miwa, K. Yoshizawa, A. Staykov and M. Yamauchi, Heterointerface Created on Au-Cluster-Loaded Unilamellar Hydroxide Electrocatalysts as a Highly Active Site for the Oxygen Evolution Reaction, *Adv. Mater.*, 2022, **34**(16), e2110552, DOI: 10.1002/adma.202110552.

4 P. C. Wang, Y. Q. Lin, L. Wan and B. G. Wang, Construction of a Janus MnO_2-NiFe Electrode via Selective Electrodeposition Strategy as a High-Performance Bifunctional Electrocatalyst for Rechargeable Zinc-Air Batteries, *ACS Appl. Mater. Interfaces*, 2019, **11**(41), 37701–37707, DOI: 10.1021/acsami.9b12232.

5 Z. L. Wang, D. Xu, J. J. Xu and X. B. Zhang, Oxygen electrocatalysts in metal-air batteries: from aqueous to nonaqueous electrolytes, *Chem. Soc. Rev.*, 2014, **43**(22), 7746–7786, DOI: 10.1039/c3cs60248f.

6 J. H. Li, Y. P. Liu, H. Chen, Z. K. Zhang and X. X. Zou, Design of a Multilayered Oxygen-Evolution Electrode with High Catalytic Activity and Corrosion Resistance for Saline Water Splitting, *Adv. Funct. Mater.*, 2021, **31**(27), 2101820, DOI: 10.1002/adfm.202101820.

7 Q. Lu, H. Wu, X. R. Zheng, Y. A. Chen, A. L. Rogach, X. P. Han, Y. D. Deng and W. B. Hu, Encapsulating Cobalt Nanoparticles in Interconnected N-Doped Hollow Carbon Nanofibers with Enriched Co–N–C Moiety for Enhanced Oxygen Electrocatalysis in Zn–Air Batteries, *Adv. Sci.*, 2021, **8**(20), 2101438, DOI: 10.1002/advs.202101438.

8 T. Z. Wang, X. J. Cao and L. F. Jiao, Ni_2P/NiMoP heterostructure as a bifunctional electrocatalyst for energy-saving hydrogen production, *eScience*, 2021, **1**(1), 69–74.

9 T. Z. Wang, X. J. Cao, H. Y. Qin, L. Shang, S. Y. Zheng, F. Fang and L. F. Jiao, P-Block Atomically Dispersed Antimony Catalyst for Highly Efficient Oxygen Reduction Reaction, *Angew. Chem., Int. Ed.*, 2021, **60**(39), 21237–21241, DOI: 10.1002/anie.202108599.

10 Y. J. Wang, B. Z. Fang, D. Zhang, A. J. Li, D. P. Wilkinson, A. Ignaszak, L. Zhang and J. J. Zhang, A Review of Carbon-Composited Materials as Air-Electrode Bifunctional Electrocatalysts for Metal-Air Batteries, *Electrochem. Energy Rev.*, 2018, **1**(1), 1–34, DOI: 10.1007/s41918-018-0002-3.

11 X. Liu, G. Zhang, L. Wang and H. Fu, Structural Design Strategy and Active Site Regulation of High-Efficient Bifunctional Oxygen Reaction Electrocatalysts for Zn-Air Battery, *Small*, 2021, **17**(48), e2006766, DOI: 10.1002/smll.202006766.

12 S. S. Ren, X. D. Duan, S. Liang, M. D. Zhang and H. G. Zheng, Bifunctional electrocatalysts for Zn-air batteries: recent developments and future perspectives, *J. Mater. Chem. A*, 2020, **8**(13), 6144–6182, DOI: 10.1039/c9ta14231b.

13 M. Busch, N. B. Halck, U. I. Kramm, S. Siahrostami, P. Krtil and J. Rossmeisl, Beyond the top of the volcano? – A unified approach to electrocatalytic oxygen reduction and oxygen evolution, *Nano Energy*, 2016, **29**, 126–135.

14 F. Calle-Vallejo, J. I. Martinez and J. Rossmeisl, Density functional studies of functionalized graphitic materials with late transition metals for Oxygen Reduction Reactions, *Phys. Chem. Chem. Phys.*, 2011, **13**(34), 15639–15643, DOI: 10.1039/c1cp21228a.

15 C. X. Zhao, J. N. Liu, J. Wang, D. Ren, B. Q. Li and Q. Zhang, Recent advances of noble-metal-free bifunctional oxygen reduction and evolution electrocatalysts, *Chem. Soc. Rev.*, 2021, **50**(13), 7745–7778, DOI: 10.1039/d1cs00135c.

16 Z. C. Yao, T. Tang, J. S. Hu and L. J. Wan, Recent Advances on Nonprecious-Metal-Based Bifunctional Oxygen Electrocatalysts for Zinc-Air Batteries, *Energy Fuels*, 2021, **35**(8), 6380–6401, DOI: 10.1021/acs.energyfuels.1c00275.

17 J. S. Kim, B. Kim, H. Kim and K. Kang, Recent Progress on Multimetal Oxide Catalysts for the Oxygen Evolution Reaction, *Adv. Energy Mater.*, 2018, **8**(11), 1702774, DOI: 10.1002/aenm.201702774.

18 M. S. Burke, M. G. Kast, L. Trotochaud, A. M. Smith and S. W. Boettcher, Cobalt-iron (oxy)hydroxide oxygen evolution electrocatalysts: the role of structure and composition on activity, stability, and mechanism, *J. Am. Chem. Soc.*, 2015, **137**(10), 3638–3648, DOI: 10.1021/jacs.5b00281.

19 G. A. Gebreslase, M. V. Martinez-Huerta and M. J. Lazaro, Recent progress on bimetallic NiCo and CoFe based electrocatalysts for alkaline oxygen evolution reaction: A review, *J. Energy Chem.*, 2022, **67**, 101–137.

20 C. G. Morales-Guio, L. Liardet and X. L. Hu, Oxidatively Electrodeposited Thin-Film Transition Metal (Oxy) hydroxides as Oxygen Evolution Catalysts, *J. Am. Chem. Soc.*, 2016, **138**(28), 8946–8957, DOI: 10.1021/jacs.6b05196.

21 D. Kowalski, H. Kiuchi, T. Motohashi, Y. Aoki and H. Habazaki, Activation of Catalytically Active Edge-Sharing Domains in Ca2FeCoO5 for Oxygen Evolution Reaction in Highly Alkaline Media, *ACS Appl. Mater. Interfaces*, 2019, **11**(32), 28823–28829, DOI: 10.1021/acsami.9b06854.

22 X. M. Liu, X. Y. Cui, K. Dastafkan, H. F. Wang, C. Tang, C. Zhao, A. B. Chen, C. X. He, M. H. Han and Q. Zhang, Recent advances in spinel-type electrocatalysts for bifunctional oxygen reduction and oxygen evolution reactions, *J. Energy Chem.*, 2021, **53**, 290–302, DOI: 10.1016/j.jechem.2020.04.012.

23 Y. Y. Liang, Y. G. Li, H. L. Wang, J. G. Zhou, J. Wang, T. Regier and H. J. Dai, Co3O4 nanocrystals on graphene as a synergistic catalyst for oxygen reduction reaction, *Nat. Mater.*, 2011, **10**(10), 780–786, DOI: 10.1038/Nmat3087.

24 X. P. Han, G. W. He, Y. He, J. F. Zhang, X. R. Zheng, L. L. Li, C. Zhong, W. B. Hu, Y. D. Deng and T. Y. Ma, Engineering Catalytic Active Sites on Cobalt Oxide Surface for Enhanced Oxygen Electrocatalysis, *Adv. Energy Mater.*, 2018, **8**(10), 1702222, DOI: 10.1002/aenm.201702222.

25 Y. Liang, H. Wang, P. Diao, W. Chang, G. Hong, Y. Li, M. Gong, L. Xie, J. Zhou, J. Wang, *et al.*, Oxygen reduction

electrocatalyst based on strongly coupled cobalt oxide nanocrystals and carbon nanotubes, *J. Am. Chem. Soc.*, 2012, **134**(38), 15849–15857, DOI: 10.1021/ja305623m.

26 A. Aijaz, J. Masa, C. Rosler, W. Xia, P. Weide, A. J. R. Botz, R. A. Fischer, W. Schuhmann and M. Muhler, Co@Co3O4 Encapsulated in Carbon Nanotube-Grafted Nitrogen-Doped Carbon Polyhedra as an Advanced Bifunctional Oxygen Electrode, *Angew. Chem., Int. Ed.*, 2016, **55**(12), 4087–4091, DOI: 10.1002/anie.201509382.

27 Y. Xiao, C. G. Hu, L. T. Qu, C. W. Hu and M. H. Cao, Three-Dimensional Macroporous NiCo2O4 Sheets as a Non-Noble Catalyst for Efficient Oxygen Reduction Reactions, *Chem.–Eur. J.*, 2013, **19**(42), 14271–14278, DOI: 10.1002/chem.201302193.

28 W. Song, Z. Ren, S. Y. Chen, Y. Meng, S. Biswas, P. Nandi, H. A. Elsen, P. X. Gao and S. L. Suib, Ni- and Mn-Promoted Mesoporous Co3O4: A Stable Bifunctional Catalyst with Surface-Structure-Dependent Activity for Oxygen Reduction Reaction and Oxygen Evolution Reaction, *ACS Appl. Mater. Interfaces*, 2016, **8**(32), 20802–20813, DOI: 10.1021/acsami.6b06103.

29 G. Wu, J. Wang, W. Ding, Y. Nie, L. Li, X. Qi, S. Chen and Z. Wei, A Strategy to Promote the Electrocatalytic Activity of Spinels for Oxygen Reduction by Structure Reversal, *Angew. Chem., Int. Ed. Engl.*, 2016, **55**(4), 1340–1344, DOI: 10.1002/anie.201508809.

30 Y. Wang, T. J. Hu, Q. Liu and L. M. Zhang, CoMn2O4 embedded in MnOOH nanorods as a bifunctional catalyst for oxygen reduction and oxygen evolution reactions, *Chem. Commun.*, 2018, **54**(32), 4005–4008, DOI: 10.1039/c8cc00870a.

31 Y. C. Liu, J. A. Koza and J. A. Switzer, Conversion of electrodeposited Co(OH)(2) to CoOOH and Co3O4, and comparison of their catalytic activity for the oxygen evolution reaction, *Electrochim. Acta*, 2014, **140**, 359–365, DOI: 10.1016/j.electacta.2014.04.036.

32 L. M. Al-Qirby, S. Radiman, C. W. Siong and A. M. Ali, Sonochemical synthesis and characterization of Co3O4 nanocrystals in the presence of the ionic liquid [EMIM][BF4], *Ultrason. Sonochem.*, 2017, **38**, 640–651, DOI: 10.1016/j.ultsonch.2016.08.016.

33 G. Fan, F. Li, D. G. Evans and X. Duan, Catalytic applications of layered double hydroxides: recent advances and perspectives, *Chem. Soc. Rev.*, 2014, **43**(20), 7040–7066, DOI: 10.1039/c4cs00160e.

34 D. Zhou, P. Li, X. Lin, A. McKinley, Y. Kuang, W. Liu, W. F. Lin, X. Sun and X. Duan, Layered double hydroxide-based electrocatalysts for the oxygen evolution reaction: identification and tailoring of active sites, and superaerophobic nanoarray electrode assembly, *Chem. Soc. Rev.*, 2021, **50**(15), 8790–8817, DOI: 10.1039/d1cs00186h.

35 O. O. Balayeva, A. A. Azizov, M. B. Muradov, R. M. Alosmanov, G. M. Eyvazova and S. J. Mammadyarova, Cobalt chromium-layered double hydroxide, alpha- and beta- $Co(OH)_2$ and amorphous $Cr(OH)_3$: Synthesis, modification and characterization, *Heliyon*, 2019, **5**(11), e02725, DOI: 10.1016/j.heliyon.2019.e02725.

36 R. Z. Ma, J. B. Liang, X. H. Liu and T. Sasaki, General Insights into Structural Evolution of Layered Double Hydroxide: Underlying Aspects in Topochemical Transformation from Brucite to Layered Double Hydroxide, *J. Am. Chem. Soc.*, 2012, **134**(48), 19915–19921, DOI: 10.1021/ja310246r.

37 Y. Aoki, E. Tsuji, T. Motohashi, D. Kowalski and H. Habazaki, $La_{0.7}Sr_{0.3}Mn_{1-x}Ni_xO_3$-delta Electrocatalysts for the Four-Electron Oxygen Reduction Reaction in Concentrated Alkaline Media, *J. Phys. Chem. C*, 2018, **122**(39), 22301–22308, DOI: 10.1021/acs.jpcc.8b06741.

38 Y. Sato, S. Kitano, D. Kowalski, Y. Aoki, N. Fujiwara, T. Ioroi and H. Habazaki, Spinel-Type Metal Oxide Nanoparticles Supported on Platelet-Type Carbon Nanofibers as a Bifunctional Catalyst for Oxygen Evolution Reaction and Oxygen Reduction Reaction, *Electrochemistry*, 2020, **88**(6), 566–573, DOI: 10.5796/electrochemistry.20-00107.

39 E. Tsuji, T. Motohashi, H. Noda, D. Kowalski, Y. Aoki, H. Tanida, J. Niikura, Y. Koyama, M. Mori, H. Arai, *et al.*, Brownmillerite-type Ca2 FeCoO5 as a Practicable Oxygen Evolution Reaction Catalyst, *Chemsuschem*, 2017, **10**(14), 2864–2868, DOI: 10.1002/cssc.201700499.

40 N. Fujiwara, T. Nagai, T. Ioroi, H. Arai and Z. Ogumi, Bifunctional electrocatalysts of lanthanum-based perovskite oxide with Sb-doped SnO2 for oxygen reduction and evolution reactions, *J. Power Sources*, 2020, **451**, 227736, DOI: 10.1016/j.jpowsour.2020.227736.

41 J. B. Liang, R. Z. Ma, N. B. O. Iyi, Y. Ebina, K. Takada and T. Sasaki, Topochemical Synthesis, Anion Exchange, and Exfoliation of Co-Ni Layered Double Hydroxides: A Route to Positively Charged Co-Ni Hydroxide Nanosheets with Tunable Composition, *Chem. Mater.*, 2010, **22**(2), 371–378, DOI: 10.1021/cm902787u.

42 Q. Wang and D. O'Hare, Recent advances in the synthesis and application of layered double hydroxide (LDH) nanosheets, *Chem. Rev.*, 2012, **112**(7), 4124–4155, DOI: 10.1021/cr200434v.

43 H. Liang, F. Meng, M. Caban-Acevedo, L. Li, A. Forticaux, L. Xiu, Z. Wang and S. Jin, Hydrothermal continuous flow synthesis and exfoliation of NiCo layered double hydroxide nanosheets for enhanced oxygen evolution catalysis, *Nano Lett.*, 2015, **15**(2), 1421–1427, DOI: 10.1021/nl504872s.

44 S. Ibraheem, S. G. Chen, J. Li, Q. M. Wang and Z. D. Wei, In situ growth of vertically aligned FeCoOOH-nanosheets/nanoflowers on Fe,N co-doped 3D-porous carbon as efficient bifunctional electrocatalysts for rechargeable zinc-O-2 batteries, *J. Mater. Chem. A*, 2019, **7**(16), 9497–9502, DOI: 10.1039/c9ta01964b.

45 Y. J. Xue, S. S. Sun, Q. Wang, Z. H. Dong and Z. P. Liu, Transition metal oxide-based oxygen reduction reaction electrocatalysts for energy conversion systems with aqueous electrolytes, *J. Mater. Chem. A*, 2018, **6**(23), 10595–10626, DOI: 10.1039/c7ta10569j.

46 C. Feng, M. B. Faheem, J. Fu, Y. Q. Xiao, C. L. Li and Y. B. Li, Fe-Based Electrocatalysts for Oxygen Evolution Reaction:

Progress and Perspectives, *ACS Catal.*, 2020, **10**(7), 4019–4047, DOI: **10.1021/acscatal.9b05445**.

47 X. Wu, C. Tang, Y. Cheng, X. Min, S. P. Jiang and S. Wang, Bifunctional Catalysts for Reversible Oxygen Evolution Reaction and Oxygen Reduction Reaction, *Chemistry*, 2020, **26**(18), 3906–3929, DOI: **10.1002/chem.201905346**.

48 M. Pourbaix, *Atlas of Electrochemical Equilibria in Aqueous Solutions*, Pergamon Press Ltd, 1966, pp. 449–457.